Intergranular Corrosion and Chromium Depletion in Low-Medium Chromium Martensitic Stainless-Steel Turbine Blades: A Thermodynamic and Metallographic Analysis

Hellen Marube Okwemba[1], Abel N. Mayaka[2], Edward O.V. Odhong[3]

[123]Multimedia University of Kenya, Faculty of Engineering and Technology

DOI: https://doi.org/10.51584/IJRIAS.2026.11060138

Received: 17 June 2026; Accepted: 22 June 2026; Published: 03 July 2026

ABSTRACT

Geothermal turbine blades manufactured from low-medium chromium stainless steel (11.5–13.5% Cr) exhibit unexpected intergranular corrosion (IGC) despite compliance with material specifications. This study investigates the mechanisms of chromium depletion and sensitization in stainless steel blades operating under geothermal conditions. Six failed blades and three operational blades from Ol-Karia II Geothermal Power Station were analysed using scanning electron microscope (SEM) fitted with energy dispersive spectrometry (EDS), X-ray diffraction (XRD), and Calculation of Phase Diagram (CALPHAD) thermodynamic modelling. Results revealed localized chromium depletion zones adjacent to grain boundaries, carbide precipitation patterns, and intergranular corrosion pathways. Thermodynamic phase diagrams predicted carbide formation temperatures and chromium diffusion profiles. Electrochemical stability diagrams showed that geothermal steam conditions (high chloride and sulphide concentrations) exceed the passivity boundaries of the tested material. This work demonstrates that intergranular corrosion in spec-compliant stainless-steel results from sensitization during manufacturing or service, exacerbated by aggressive geothermal fluid chemistry.

Keywords: Inter-granular Corrosion, Geothermal Turbines, Sensitization, CALPHAD, Thermodynamics

INTRODUCTION

Geothermal energy production is increasingly recognised as a vital component of sustainable power generation, yet its reliability depends heavily on the durability of turbine blades exposed to extreme operating conditions [1,2]. These blades must withstand high temperatures in the range of 150–250°C, elevated pressures, and corrosive steam chemistries rich in chlorides, sulphides, and non-condensable gases [3,4]. Low-medium chromium stainless steels containing 11.5–13.5% Cr are often selected for their cost-effectiveness and compliance with ASTM and ISO specifications [5]. However, field evidence from geothermal plants such as Ol-Karia II in Kenya reveals that these alloys are vulnerable to intergranular corrosion (IGC), a degradation mode that undermines efficiency, increases maintenance costs, and shortens service life [6,7].

Intergranular corrosion arises when chromium-depleted zones form along grain boundaries, typically due to carbide precipitation during welding or thermal exposure [8,9]. In geothermal environments, sensitisation is accelerated by aggressive fluid chemistries that destabilise the passive film [8,10–12]. While sensitisation mechanisms have been extensively studied in high-chromium austenitic stainless steels (>17% Cr) [13–16], the behaviour of low-medium chromium alloys under geothermal conditions remains poorly understood. This gap is significant because these alloys are widely deployed in African geothermal plants, yet their long-term reliability is uncertain [17].

Previous research has established that chromium depletion adjacent to grain boundaries is the primary driver of sensitisation and IGC [18–20]. Studies on austenitic stainless steels have shown that carbide precipitation during thermal cycling reduces local chromium concentrations below the passivation threshold, thereby exposing grain

boundaries to corrosive attack [21–24]. Thermodynamic modelling approaches, such as CALPHAD, have been used to predict carbide formation temperatures and diffusion profiles, while metallographic techniques (SEM/EDS, XRD) have validated microstructural changes [25–27]. Electrochemical stability diagrams have also been applied to stainless steels in chloride environments, demonstrating how aggressive chemistries destabilise passive films [28].

Despite these advances, the literature is dominated by investigations of high-chromium alloys[13,14]. Research on geothermal turbine failures has tended to emphasise general corrosion, erosion, and scaling, with limited attention to intergranular phenomena in low-medium chromium steels. Moreover, few studies have integrated thermodynamic modelling with metallographic validation to provide a comprehensive picture of chromium depletion in service-exposed blades [29–31]. Electrochemical stability diagrams have rarely been applied to geothermal steam chemistries [32], leaving a gap in understanding how chloride and sulphide concentrations interact with sensitised microstructures.

Three critical gaps emerge from the literature. First, the material scope is limited: most studies focus on high-chromium stainless steels, leaving low-medium chromium alloys insufficiently characterised despite their widespread use in geothermal turbines. Second, there is a lack of mechanistic clarity: the precise pathways of chromium depletion and sensitisation in geothermal environments have not been systematically mapped, particularly the interplay between carbide precipitation and aggressive fluid chemistry. Third, there is a methodological gap: few studies combine thermodynamic modelling (CALPHAD, electrochemical diagrams) with metallographic validation (SEM/EDS, XRD) to provide a holistic understanding of IGC in service-exposed blades.

This study addresses these gaps by investigating failed and operational blades from Ol-Karia II Geothermal Power Station using a mixed methodological approach. Six failed blades and three operational blades were analysed through SEM/EDS, XRD, and CALPHAD thermodynamic modelling. The integration of experimental and modelling techniques provides a robust framework for characterising chromium depletion zones, carbide precipitation patterns, and intergranular corrosion pathways. Electrochemical stability diagrams were further employed to assess the passivity boundaries of the tested material under geothermal steam conditions. The novelty of this research lies in its focus on low-medium chromium stainless steels, a class of materials that has been overlooked in geothermal corrosion studies. By demonstrating that intergranular corrosion can occur in alloys that meet specification standards, the study challenges assumptions about material compliance and reliability. The findings refine understanding of sensitisation mechanisms, showing how manufacturing processes and service exposure interact with geothermal fluid chemistry to exacerbate corrosion.

The contribution is threefold. Scientifically, the study provides mechanistic clarity on chromium depletion and sensitisation in low-medium chromium stainless steels, integrating thermodynamic predictions with metallographic evidence. Methodologically, it demonstrates the value of combining CALPHAD modelling, electrochemical stability diagrams, and microstructural analysis to capture both predictive and empirical dimensions of corrosion. Practically, it offers actionable insights for geothermal plant operators, highlighting the need to reconsider material selection, manufacturing practices, and maintenance protocols for turbine blades.

MATERIALS AND METHODS

The materials and methods employed in this study were designed to capture both the microstructural and thermodynamic mechanisms underlying intergranular corrosion in low-medium chromium stainless steel turbine blades. Six failed blades, designated F01–F06, and three operational blades, designated G01–G03, were randomly selected from Ol-Karia II Geothermal Power Station. Each blade was sectioned and prepared for metallographic examination through sequential grinding with 220–600 grit papers, polishing with diamond pastes ranging from 6 to 1 μm, and etching in a solution of 10% nitric acid in methanol. This preparation ensured that grain boundaries, carbide precipitates, and corrosion features were clearly revealed for subsequent analysis. Figure 1 illustrates the study framework.

ISSN No. 2454-6194 | DOI: 10.51584/IJRIAS |Volume XI Issue VI June 2026

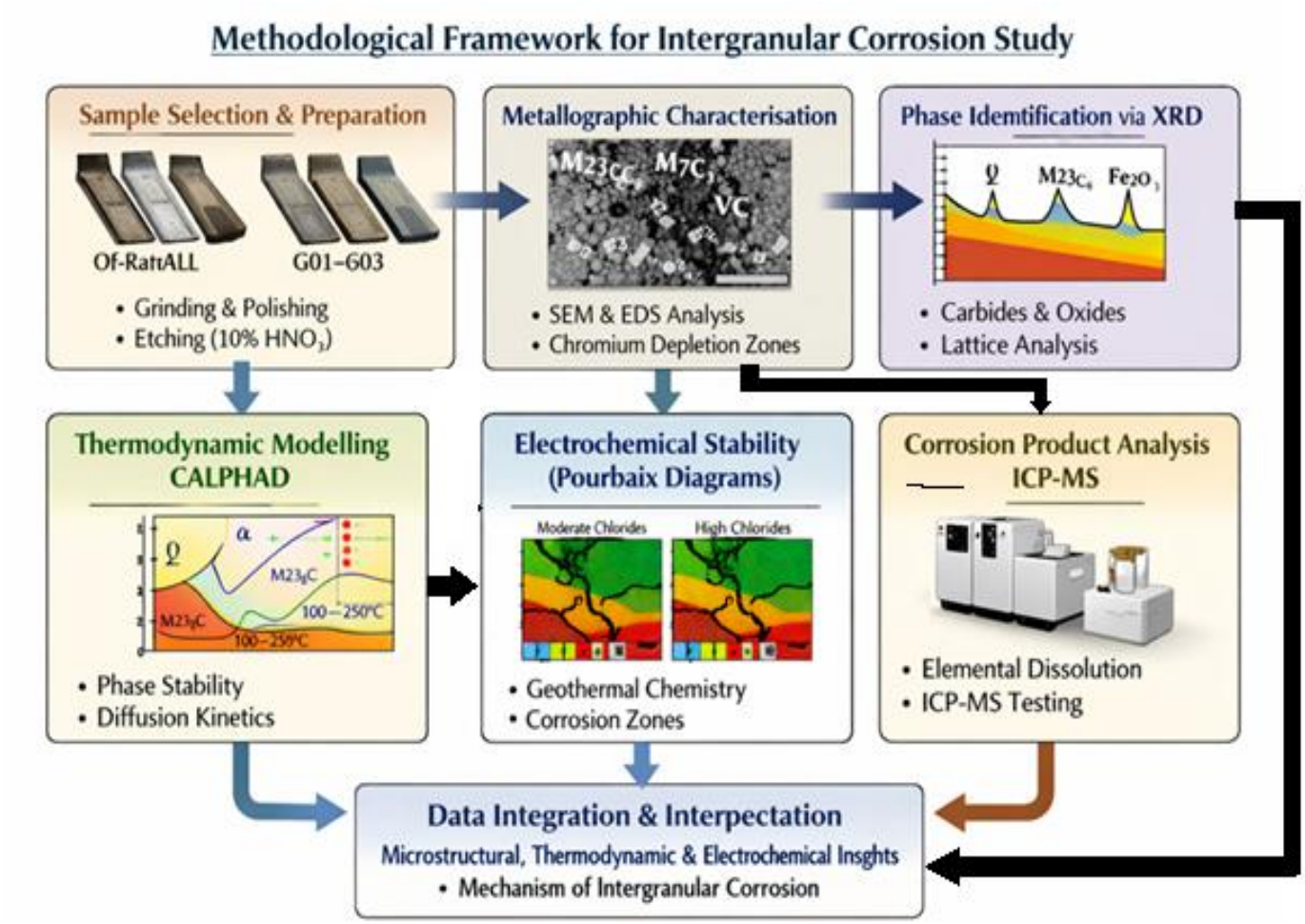

Figure 1: Framework for the study

Metallographic characterisation was conducted using SEM coupled with EDS. SEM imaging was performed at magnifications between 500× and 5000× to capture both general microstructural features and fine details of grain boundary attack. EDS elemental mapping was applied across grain boundaries and corrosion sites to quantify chromium, iron, nickel, and molybdenum distributions. These profiles provided direct evidence of chromium depletion zones adjacent to carbides and corrosion pathways. Complementary phase identification was achieved through X-ray diffraction, which enabled the detection of corrosion products and carbide phases, as well as lattice parameter analysis to assess subtle structural changes.

Thermodynamic modelling was undertaken using the CALPHAD approach to predict phase stability within the geothermal operating range of 100–250°C. The alloy composition was defined as 11.5–13.5% chromium, 8–10% nickel, with the balance iron. The modelling predicted the stability of austenite and ferrite phases, alongside the formation of $M_{23}C_6$ and M_7C_3 carbides. Chromium diffusion behaviour was simulated using Fick's second law with temperature-dependent diffusion coefficients, allowing the kinetics of carbide precipitation and chromium depletion to be assessed. Electrochemical stability diagrams (Pourbaix diagrams) were constructed to reflect geothermal fluid conditions, incorporating chloride and sulphide concentrations measured from steam analysis. These diagrams provided insight into the passivity boundaries of the alloy and the conditions under which passive films break down.

To complement microstructural and modelling data, corrosion product analysis was performed. Corrosion deposits were dissolved in dilute hydrochloric acid, and the resulting solutions were analysed using inductively coupled plasma mass spectrometry. Inductively coupled plasma mass spectrometry (ICP-MS) quantified the dissolution rates of iron, chromium, nickel, and molybdenum, thereby linking microstructural degradation to elemental loss. This multi-method approach—combining metallography, thermodynamics, electrochemistry, and chemical analysis—ensured that both the mechanisms and consequences of intergranular corrosion were comprehensively characterised.

ISSN No. 2454-6194 | DOI: 10.51584/IJRIAS |Volume XI Issue VI June 2026

RESULTS

The metallographic analysis revealed clear evidence of intergranular corrosion in the failed blades compared to the operational samples. SEM/EDS imaging showed corrosion pathways penetrating 10–50 μm along grain boundaries in blades F01–F06. Chromium concentrations at these boundaries were significantly depleted, averaging 6–8%, compared to the bulk alloy composition of 11.5–13.5%. This depletion is consistent with sensitisation caused by carbide precipitation. In contrast, operational blades G01–G03 displayed uniform chromium distribution across the matrix, with no evidence of depletion zones. Carbide phases identified at grain boundaries included $M_{23}C_6$ and M_7C_3, both of which are known to consume chromium during precipitation and thereby destabilise passive films. Figure 2 illustrates SEM/EDS for damaged blades.

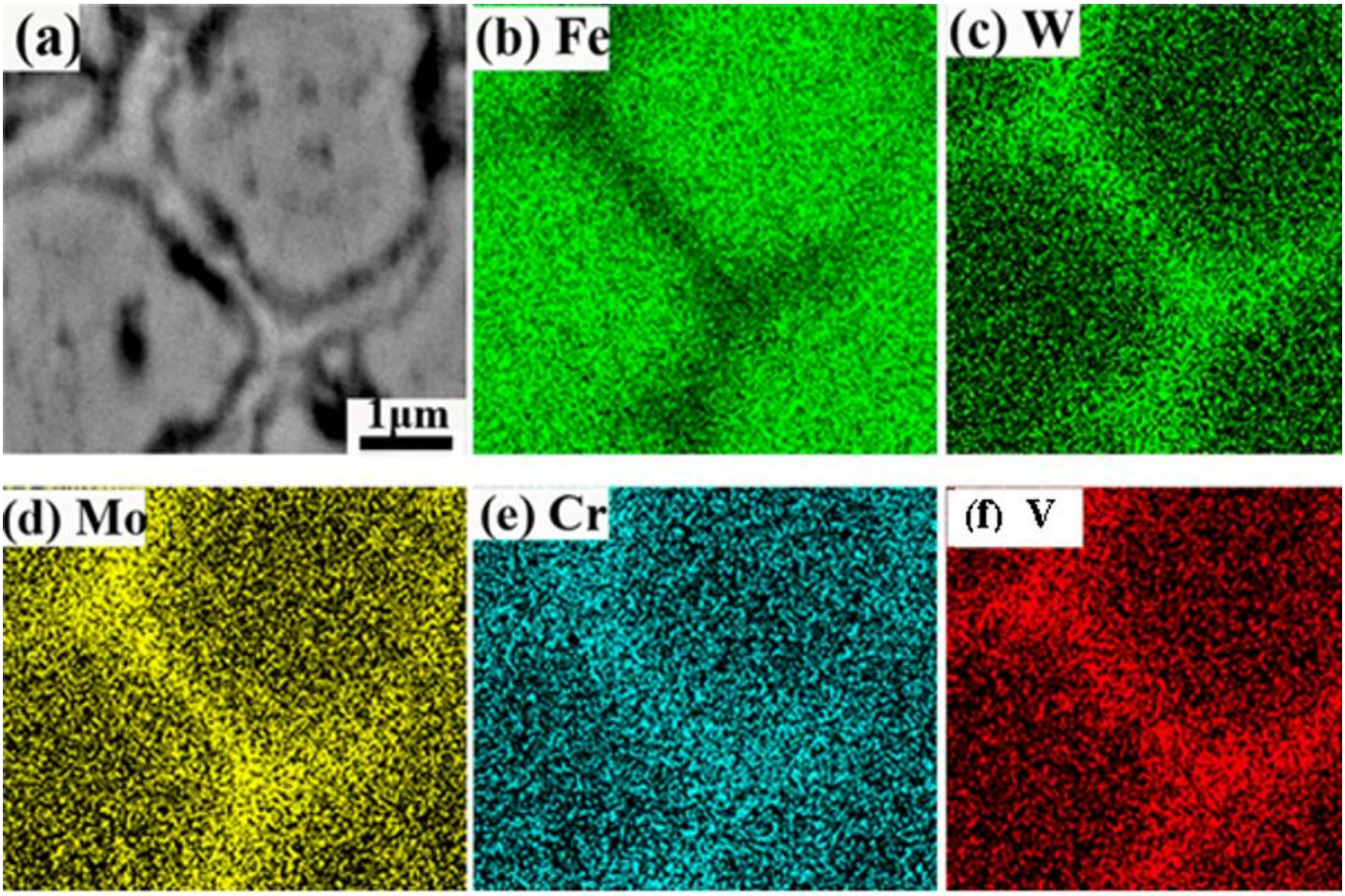

Figure 2: SEM/EDS images of damaged blade (a) SEM image showing cracks and grain-boundaries (b) EDS confirming iron (c) EDS confirming tungsten (d) EDS confirming molybdenum (e) EDS confirming chromium and (f) EDS confirming vanadium.

XRD analysis further corroborated these findings. Failed blades exhibited a multiphase structure consisting of austenite, face-centered cubic chromium carbide ($M_{23}C_6$) phase, hexagonal chromium carbide phase (M_7C_3) phase, and iron oxides, indicating both sensitisation and secondary oxidation. Operational blades, however, showed only austenitic phases, confirming the absence of carbide precipitation and corrosion products. These results demonstrate that intergranular corrosion is strongly associated with chromium depletion and carbide formation, processes absent in blades that remain in service. Figure 3 illustrates XRD results that capture the contrast between failed and operational stainless-steel turbine blades. The upper red plot represents the failed blades, showing multiple diffraction peaks corresponding to austenite (γ), carbide phases ($M_{23}C_6$ and M_7C_3), and iron oxides (Fe_2O_3/Fe_3O_4). These multiphase signatures confirm sensitisation and secondary oxidation, consistent with chromium depletion and carbide precipitation at grain boundaries. The lower blue plot, representing operational blades, displays only austenitic peaks, indicating a single-phase structure free from carbides or oxides.

ISSN No. 2454-6194 | DOI: 10.51584/IJRIAS |Volume XI Issue VI June 2026

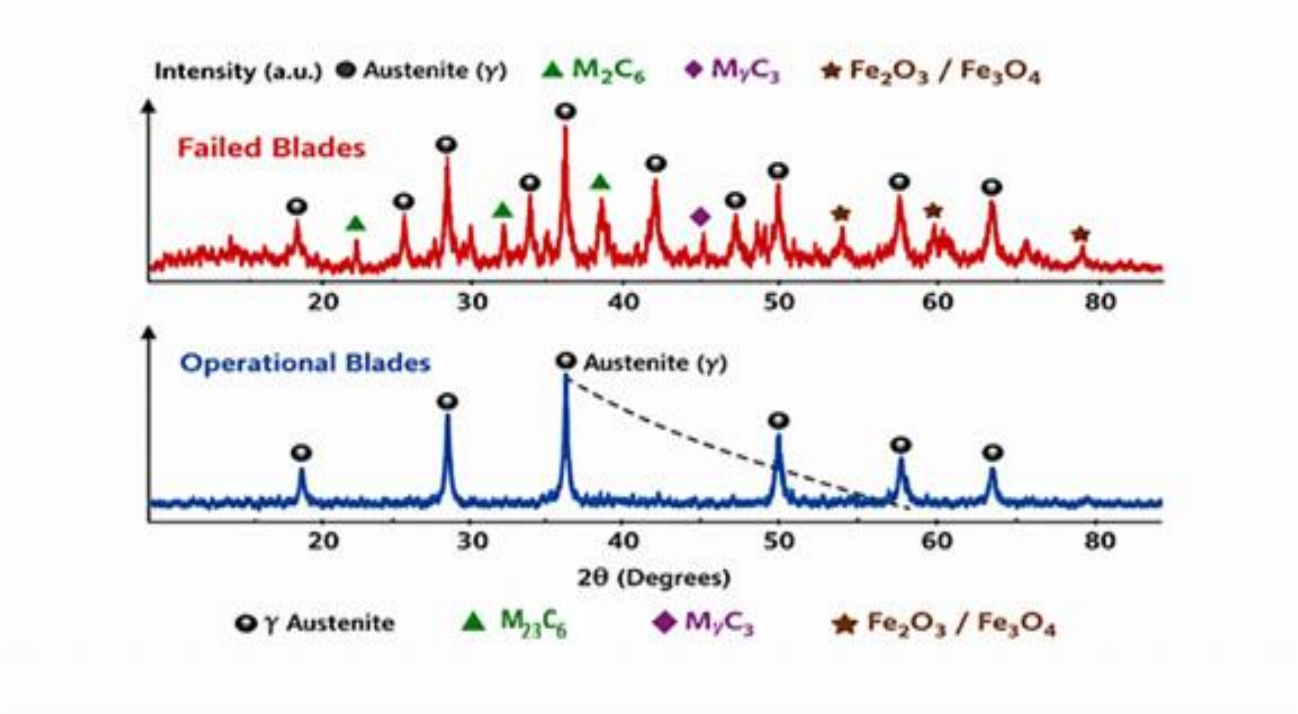

Figure 3: Results of XRD analysis of failed and operational blades

Thermodynamic modelling provided predictive support for the experimental observations. CALPHAD phase diagrams in Figure 4 indicated that carbide precipitation occurs at temperatures above 150°C for the tested composition, aligning with geothermal operating conditions. Chromium diffusion modelling at 200°C yielded a rate of approximately 10^{-15} m²/s, predicting sensitisation depths of 5–20 µm. These values closely matched the SEM observations of 10–50 µm corrosion pathways, validating the modelling approach.

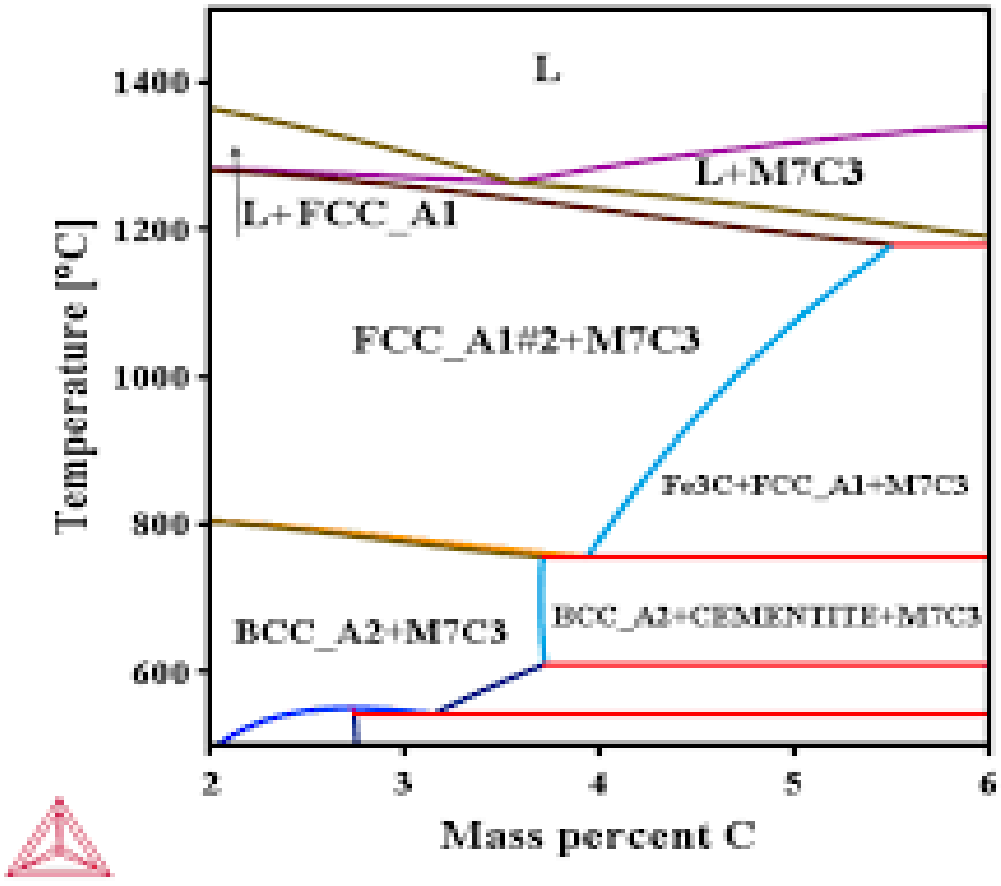

Figure 4: Thermocalc diagram for phase diagram

ISSN No. 2454-6194 | DOI: 10.51584/IJRIAS |Volume XI Issue VI June 2026

The Pourbaix diagrams constructed for geothermal fluid conditions (pH 6–8, chloride concentrations of 500–2000 ppm, and sulphide concentrations of 50–200 ppm) placed chromium in the corrosion region. This indicates that the passive film stability is exceeded under geothermal steam chemistry, particularly in chromium-depleted zones.

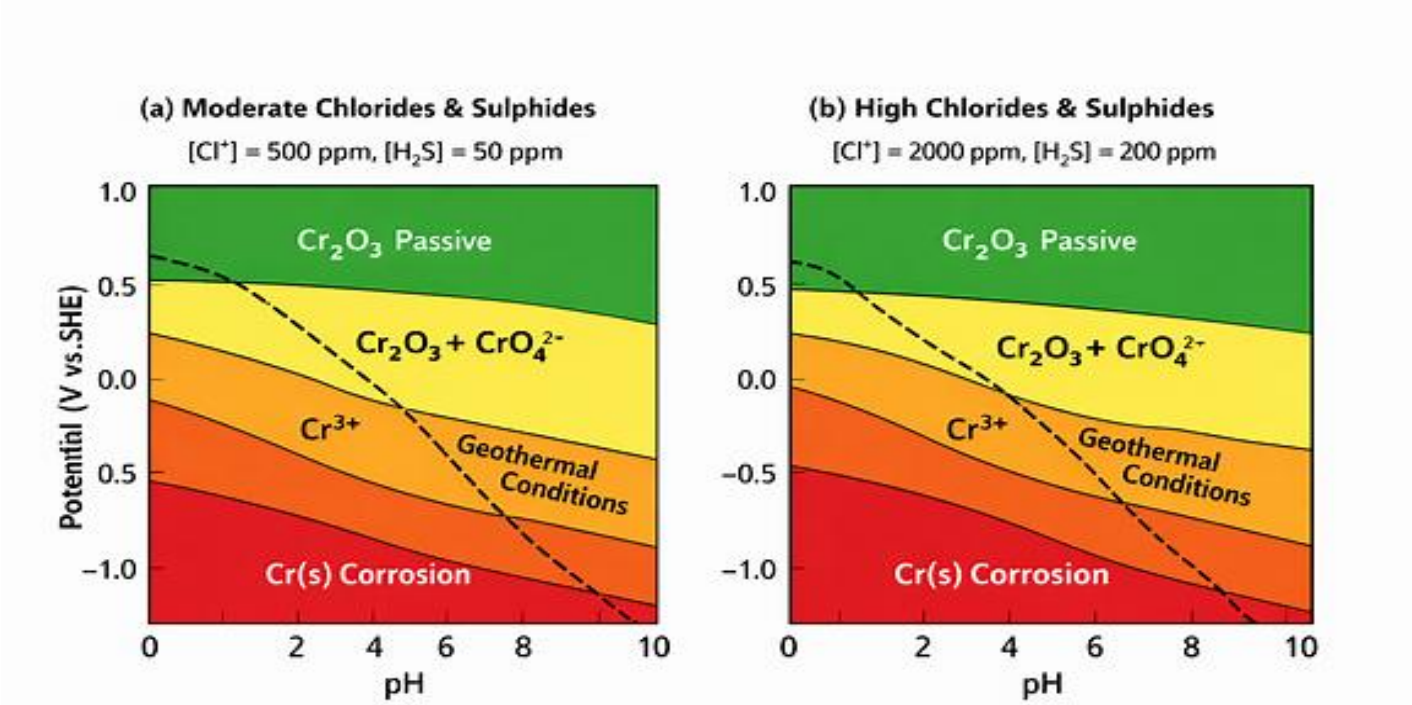

Figure 3: Pourbaix diagrams for chromium under geothermal conditions.

Figure 5: Pourbaix diagrams (a) Moderate chlorides and sulphides and (b) high chlorides and sulphides

In Figure 5**,** the left panel (a) represents moderate geothermal chemistry ($[Cl^-] \approx 500$ ppm, $[H_2S] \approx 50$ ppm), where the operating potential line intersects the boundary between the Cr_2O_3 passive region and the Cr^{3+} dissolution zone. This indicates marginal stability of the passive film under typical geothermal conditions. The right panel (b) depicts high chloride and sulphide concentrations ($[Cl^-] \approx 2000$ ppm, $[H_2S] \approx 200$ ppm), where the operating line lies entirely within the corrosion region, confirming that aggressive steam chemistry overwhelms the protective oxide layer.

Electrochemical analysis quantified the corrosion rates, revealing stark contrasts between bulk material and grain boundary regions. The bulk alloy exhibited corrosion rates of 0.1–0.5 mm/year, consistent with acceptable service performance. However, grain boundary regions showed accelerated rates of 2–5 mm/year, representing a 10–50× increase. This acceleration explains the premature failure of blades despite compliance with specifications. The localisation of corrosion at grain boundaries highlights the critical role of chromium depletion in driving intergranular attack.

Table 1. Chromium Concentration and Corrosion Depth

Blade Type	Chromium at Grain Boundaries (%)	Bulk Chromium (%)	Corrosion Pathway Depth (μm)	Phases Identified
Failed (F01–F06)	6–8	11.5–13.5	10–50	Austenite + $M_{23}C_6$ + M_7C_3 + Fe oxides
Operational (G01–G03)	11.5–13.5	11.5–13.5	None	Austenite only

DISCUSSIONS

The convergence of metallographic, thermodynamic, and electrochemical evidence demonstrates that intergranular corrosion in low-medium chromium stainless steels is driven by sensitisation and exacerbated by geothermal fluid chemistry. Chromium depletion was quantified both experimentally and through modelling. The depletion of chromium at grain boundaries due to carbide precipitation reduces local concentrations below the passivity threshold, exposing boundaries to corrosive attack. EDS profiles revealed chromium concentrations of 6–8% at grain boundaries compared to 11.5–13.5% in the bulk alloy. CALPHAD predictions and diffusion modelling confirmed that chromium concentrations fall below the minimum threshold required for passivity. This depletion explains why grain boundaries lose their protective film even though the bulk alloy remains compliant with specifications. This was consistent with the thermodynamic predictions reported in previous research [25–27].

The Pourbaix diagrams constructed in the research also extend prior electrochemical studies [28,32]. Earlier work demonstrated passive film destabilisation in chloride environments, but rarely under geothermal steam chemistries. The diagrams reveal that chloride and sulphide concentrations typical of Ol-Karia II place chromium in the corrosion region, confirming that geothermal fluids exceed passivity boundaries. This corroborates the methodological gap noted in the Introduction, where electrochemical stability diagrams had not been applied to geothermal steam. Electrochemical data quantify the dramatic acceleration of corrosion at grain boundaries, explaining why blades fail prematurely despite specification compliance.

This study challenges the assumption that specification compliance guarantees reliability. While earlier investigations emphasised high-chromium alloys [13–16]. Evidence from this study demonstrates that low-medium chromium steels are equally vulnerable to sensitisation under geothermal conditions. For geothermal operators, the results underscore the need to reconsider material selection, manufacturing practices, and maintenance protocols. For researchers, the integration of SEM/EDS, XRD, CALPHAD modelling, and electrochemical analysis provides a methodological template for studying corrosion in complex environments.\

CONCLUSIONS

This study demonstrates that intergranular corrosion in spec-compliant low-medium chromium stainless steel turbine blades is driven by sensitization (carbide precipitation and chromium depletion) combined with aggressive geothermal fluid chemistry. Thermodynamic modelling successfully predicts carbide formation and chromium diffusion profiles, validating metallographic observations. The 10–50× acceleration of corrosion at grain boundaries explains field failure rates. A layered strategy to strengthen turbine blade resilience is recommended. Material upgrade should prioritise alloys with chromium content above 16 % or shift toward nickel-based superalloys to resist sensitisation. Surface protection through ceramic or thermal-barrier coatings can shield grain boundaries from corrosive geothermal fluids. Operational controls must focus on lowering chloride and sulphide levels in steam via improved separation and treatment systems, thereby reducing electrochemical attack. Finally, monitoring using eddy-current testing will enable early detection of sensitisation and microcrack formation, ensuring blades are replaced before catastrophic failure.

REFERENCES

[1] O.I. Balytskyi, L.M. Ivaskevych, Effect of soldering process parameters on hydrogen embrittlement of austenitic-martensitic steels, Strength Mater (2026). https://doi.org/10.1007/s11223-026-00898-2.

[2] Z. Xing, N. Wang, L. Fan, L. Shang, L. Yu, Investigation of the corrosion performance of HVOF-sprayed WC-CoCr coatings applied on offshore hydraulic equipment, REVIEWS ON ADVANCED MATERIALS SCIENCE 64 (2025) 20240066. https://doi.org/10.1515/rams-2024-0066.

[3] A.N. Kamau, P.K. Gevera, Evaluation of silica scaling potential for selected wells within Olkaria Domes Geothermal Field, Nakuru County, Kenya, (2026). https://repository.dkut.ac.ke:8080/xmlui/handle/123456789/21589 (accessed June 4, 2026).

[4] J. Thevakumar, J. Owen, K. Purnell, E. Barmatov, R. Barker, Assessment of carbon steel and corrosion resistant alloy corrosion in geothermal environments containing sulphuric acid, Corrosion Science (2025)

113319. https://www.sciencedirect.com/science/article/pii/S0010938X2500647X (accessed June 4, 2026).

[5] L. Zhao, Y. Xia, T. Liu, P. Fu, Y. Zhao, J. Ren, P. Cheng, Z. Yang, Innovative Laser Cladding System for Internal and External Ni Coating of OCTG as a Cost-Effective Alternative to Solid Ni Alloys, in: CONFERENCE 2026, Association for Materials Protection and Performance, 2026: pp. 1–11. https://content.ampp.org/ampp/proceedings/CONF_MAR26/2026/1/107266 (accessed June 4, 2026).

[6] R.G. Tayactac, B. Basilia, Corrosion in the geothermal systems: a review of corrosion resistance alloy (CRA) weld overlay cladding applications, in: IOP Conference Series: Earth and Environmental Science, IOP Publishing, 2022: p. 012018. https://iopscience.iop.org/article/10.1088/1755-1315/1008/1/012018/meta (accessed June 4, 2026).

[7] T. Persico, Corrosion behavior of advanced and recovered materials for aggressive industrial environments, (2026). https://tesidottorato.depositolegale.it/bitstream/20.500.14242/365143/1/PersicoTommaso_Tesididottorato.pdf (accessed June 4, 2026).

[8] A.M. Oladoye, T. Olusanya, L.O. Osoba, Susceptibility of SMAW AISI304SS welded joints to intergranular corrosion after post-weld thermal ageing, Research in Materials Science 1 (2025) 2513705. https://doi.org/10.1080/30654327.2025.2513705.

[9] S. Kumar, A.S. Shahi, V. Sharma, D. Malhotra, Metallurgical, mechanical, and corrosion behavior of AISI 304L joints welded using variable arc energy inputs and subjected to thermal aging, Proceedings of the Institution of Mechanical Engineers, Part L: Journal of Materials: Design and Applications 238 (2024) 1981–1998. https://doi.org/10.1177/14644207241238200.

[10] D. Martelo, E. Abedi Esfahani, N. Kale, T. Maccio, S. Paul, Investigation of Scaling and Materials' Performance of EHLA-Fabricated Cladding in Simulated Geothermal Brine, Coatings 15 (2025) 1366. https://www.mdpi.com/2079-6412/15/12/1366 (accessed June 4, 2026).

[11] P.K. Verma, H. Vasudev, Surface Properties Using Fabrication of Composites for Turbine Blades, Microwave Processing of Metallic Materials (n.d.) 54–74. https://api.taylorfrancis.com/content/chapters/edit/download?identifierName=doi&identifierValue=10.1201/9781003614081-4&type=chapterpdf (accessed June 4, 2026).

[12] T. Ngwenya, A. Nava, P.T. Ireland, A Review of Secondary Combustion on Turbine Blade Cooling, Turbo Expo: Power for Land, Sea, and Air 87998 (2024) V007T11A001. https://asmedigitalcollection.asme.org/GT/proceedings-abstract/GT2024/87998/1204175 (accessed June 4, 2026).

[13] S.N. Karlsdóttir, T. Jonsson, A. Stefánsson, Corrosion behavior of high alloy austenitic stainless steel in simulated high temperature geothermal environment, in: CORROSION 2017, Association for Materials Protection and Performance, 2017: pp. 1–12. https://content.ampp.org/nace/proceedings/CONF_MAR2017/2017/1/57818 (accessed June 4, 2026).

[14] R. Bäßler, J. Sobetzki, S. Le Manchet, Corrosion Resistance of the Super-Austenitic Stainless Steel UNS S31266 for Geothermal Applications, in: CORROSION 2017, Association for Materials Protection and Performance, 2017: pp. 1–11. https://content.ampp.org/nace/proceedings/CONF_MAR2017/2017/1/57589 (accessed June 4, 2026).

[15] M. Liu, Z. Ni, C. Du, Z. Liu, M. Sun, E. Fan, Q. Wang, X. Yang, X. Li, Failure investigation of a 304 stainless steel geothermal tube, Engineering Failure Analysis 129 (2021) 105694. https://www.sciencedirect.com/science/article/pii/S1350630721005550 (accessed June 4, 2026).

[16] S. Ouahid, Investigation of microstructural changes and micro hardness of Nimonic 80A turbine blades after extended service and heat treatment, Canadian Metallurgical Quarterly (2025) 1–15. https://doi.org/10.1080/00084433.2025.2572136.

[17] M.J.B. Kabeyi, A.O. Olanrewaju, Geothermal power generation options and technologies, in: Presented at the 2nd Australian International Conference on Industrial Engineering and Operations Management, 2023: p. 242. https://www.researchgate.net/profile/Dr-Kabeyi/publication/378799672_Geothermal_Power_Generation_Options_and_Technologies/links/662672fd39e7641c0be0cb53/Geothermal-Power-Generation-Options-and-Technologies.pdf (accessed June 4, 2026).

[18] W. Zhang, W. Mao, J. Hong, X. Jin, G. Wu, Insights into the effect of Cr on interfacial and grain boundaries oxidation in Fe-Mn-Si-based alloys, Corrosion Science 244 (2025) 112638. https://www.sciencedirect.com/science/article/pii/S0010938X24008357 (accessed June 4, 2026).

[19] L. Yang, H. Qian, X. Hao, W. Kuang, The effects of grain boundary structure and bulk Cr content on grain boundary degradation behavior of Ni-Cr binary alloys in high temperature CO2, Acta Materialia 263 (2024) 119496. https://www.sciencedirect.com/science/article/pii/S135964542300825X (accessed June 4, 2026).

[20] F. Xue, E.A. Marquis, Role of diffusion-induced grain boundary migration in the oxidation response of a Ni-30 Cr alloy, Acta Materialia 240 (2022) 118343. https://www.sciencedirect.com/science/article/pii/S1359645422007224 (accessed June 4, 2026).

[21] J. Bai, H. Li, G. Wang, Review on Evolution of Oxide Layer and Chromium Depletion Layer of Austenitic Stainless Steel during Industrial Processing, Steel Research Int. 96 (2025) 13–32. https://doi.org/10.1002/srin.202400938.

[22] G. Kim, J. Lee, S. Kim, Y. Kang, J.-Y. Park, S.-W. Song, Evaluation of Sensitization Behaviors on the Heat-Affected Zone of Austenitic Stainless Steel Weld by Thermal Cycles of Actual Multi-pass Welding, Met. Mater. Int. 30 (2024) 2655–2667. https://doi.org/10.1007/s12540-024-01679-9.

[23] P. Dai, S. Li, L. Wu, Y. Wang, G. Feng, D. Deng, A new numerical model to predict welding-induced sensitization in SUS304 austenitic stainless steel joint, Journal of Materials Research and Technology 17 (2022) 234–243. https://www.sciencedirect.com/science/article/pii/S2238785422000151 (accessed June 4, 2026).

[24] I.U. Toor, Advances in Understanding of Secondary Phases and Their Corrosion Implications in Stainless Steel Alloys—A Review, Corrosion and Materials Degradation 7 (2026) 9. https://www.mdpi.com/2624-5558/7/1/9 (accessed June 4, 2026).

[25] M. Raoof, From Atom to Abyss: An Anatomical Analysis of Coating Degradation Mechanisms in Extreme Environments and Industrial Solutions, in: Advanced Coating and Cladding Technologies, CRC Press, 2026: pp. 58–87. https://api.taylorfrancis.com/content/chapters/edit/download?identifierName=doi&identifierValue=10.1201/9781003653226-3&type=chapterpdf (accessed June 4, 2026).

[26] S. Arun, N. Radhika, B. Saleh, Effect of Additional Alloying Elements on Microstructure and Properties of AlCoCrFeNi High Entropy Alloy System: A Comprehensive Review, Met. Mater. Int. 31 (2025) 285–324. https://doi.org/10.1007/s12540-024-01752-3.

[27] G. Oppong Boakye, L.E. Geambazu, A.M. Ormsdottir, B.G. Gunnarsson, I. Csaki, F. Fanicchia, D. Kovalov, S.N. Karlsdottir, Microstructural properties and wear resistance of Fe-Cr-Co-Ni-Mo-based high entropy alloy coatings deposited with different coating techniques, Applied Sciences 12 (2022) 3156. https://www.mdpi.com/2076-3417/12/6/3156 (accessed June 4, 2026).

[28] J. Muhammad Yelwa, H. Musa, O.O. Fasanya, J. Yusuf Yahaya, Corrosion-resistant coatings: advances in deposition methods, nanostructures, and self-healing films, Academia Materials Science 2 (2025). https://doi.org/10.20935/AcadMatSci7829.

[29] N.S. Zainuddin, W.F.H.W. Zamri, M.Z. Omar, M.F. bin Md Din, Comprehensive insight into the failure mechanisms, modes, and material selection of steam turbine blades, Journal of Current Science and Technology 14 (2024) 47–47. https://ph04.tci-thaijo.org/index.php/JCST/article/view/2548 (accessed June 4, 2026).

[30] N.S. Zainuddin, W.F.H.W. Zamri, M.Z. Omar, M.F. Bin Md Din, A.A. Bin Pauzi, Erosion in steam turbines: A comprehensive bibliometric and systematic review unveiling cutting-edge technologies, J Mech Sci Technol 39 (2025) 567–585. https://doi.org/10.1007/s12206-025-0106-8.

[31] G.P. Domínguez, H.M. Aviña, O. Ruiz, E.I. Ramírez, C. Reyes-Ruiz, FEM mechanical analysis of an adapted turbocharger for a low enthalpy geothermal cycle, (n.d.). https://somim.org.mx/memorias/memorias2024/articulos/DM/A1_24.pdf (accessed June 4, 2026).

[32] F. Furcas, B. Lothenbach, S. Mundra, O.B. Isgor, M.R. Geiker, U.M. Angst, Thermodynamic modeling: Success in cement science–Untapped potential in corrosion research, RILEM Technical Letters 10 (2025) 1–14. https://letters.rilem.net/index.php/rilem/article/view/214 (accessed June 4, 2026).